Implementation of AC current-sensor-less control and high-frequency modulation of an all-SiC Current Source Inverter

Yonghwa Lee, and Alberto Castellazzi
Solid-State Power Processing (SP2) Lab.,
Kyoto University of Advanced Science, Kyoto, Japan
2021md04@kuas.ac.jp; alberto.castellazzi@kuas.ac.jp

***Abstract*-- The deployment of high-frequency wide-band-gap semiconductors, such as silicon carbide MOSFETs, has renewed interest in current source inverters for advanced motor-drive systems. With higher power density and potential benefits for high-speed controllers, a high switching frequency requires high-performance digital processors. However, conventional modulation strategies derived from standard voltage-source inverters are not applicable, and precautions must be taken to prevent overvoltage and inter-phase short circuits through proper overlap and dead times. Previous studies have proposed a simplified ac current-sensor-less high-speed controller design using high switching frequency in both continuous and discrete time domains. This paper presents the physical hardware implementation and testing of this design.**

***Index Terms* — current source inverter, wide-band-gap semiconductor, ac current sensor-less, high-speed controller.**

I. INTRODUCTION

The deployment of wide-band-gap (WBG) power semi-conductors has led to a resurgence of interest in the current source inverter (CSI) due to its potential for best-in-class power densities. Traditional voltage source inverters (VSI) using silicon (Si) experience issues such as motor terminal over-voltages, common-mode emissions, and degradation of bearing and insulation when fast-switching WBG devices are used. Additionally, switching ripple current limits the reduction of DC link capacitor volume, and high common-mode emissions can lead to bearing race pitting failures. In contrast, the CSI output voltage is sinusoidal with low common-mode EMI characteristics due to the output filter capacitor [1, 2].

Fig. 1(a) shows a circuit diagram of a CSI-based motor application using DC input power. The inverter-based motor system typically controls motor torque as a load but may also need to operate in generation mode. Therefore, bi-directional switches capable of providing bi-directional power flow are necessary, as illustrated in Fig. 1(b). The bi-directional switches (BDS) used in a CSI require a different PWM strategy than those in a conventional VSI, including overlap times tailored to the semiconductor characteristics to prevent potentially destructive overvoltage caused by open circuits. Ad-hoc switching sequences, including dead times to avoid shoot-throughs, have been proposed [3].

Compared to the VSI, the CSI plant model is more complex due to the presence of a filter capacitor, as illustrated in Fig. 2(a). Typically, the plant can be represented simply using a two-stage model, as shown in Fig. 2(b). However, the plant has a resonant component due to the inductance and filter capacitor, resulting in a second-order system. Therefore, conventional CSI controllers require additional voltage sensors in the current controller to achieve wide bandwidth, as depicted in Figure 2(c). Many of the CSI control strategies utilized in AC motor drives publications employ a multi-nested-loop structure, which significantly amplifies control complexity, necessitates extra sensors, and only offers a limited enhancement in control bandwidth [4, 5].

Nevertheless, a recent study proposed a robust ac-voltage sensor-less controller design using high-speed switching and controllers [6]. By leveraging the high-switching capability of wide-band-gap semiconductors, the current controller can be simplified with robust characteristics. The bulk filter capacitors in IGBT-based conventional current source inverters lead to low resonant frequency, but advanced CSI with wide-band-gap technology can reduce the capacitance of filter capacitors, allowing the controller to have a wide control band even with only a resonant controller.

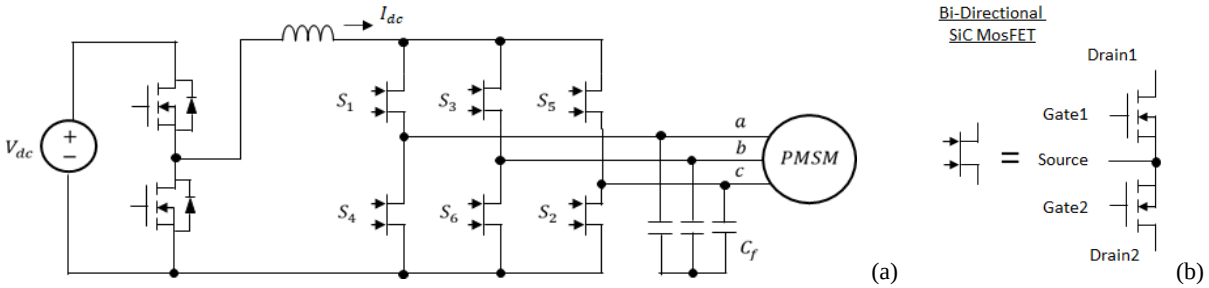

Fig. 1: (a) Circuit schematic of Buck CSI-fed PMSM using Wide-Band-Gap Bi-directional Switches and (b) schematic of MOSFET BDS in common source configuration.

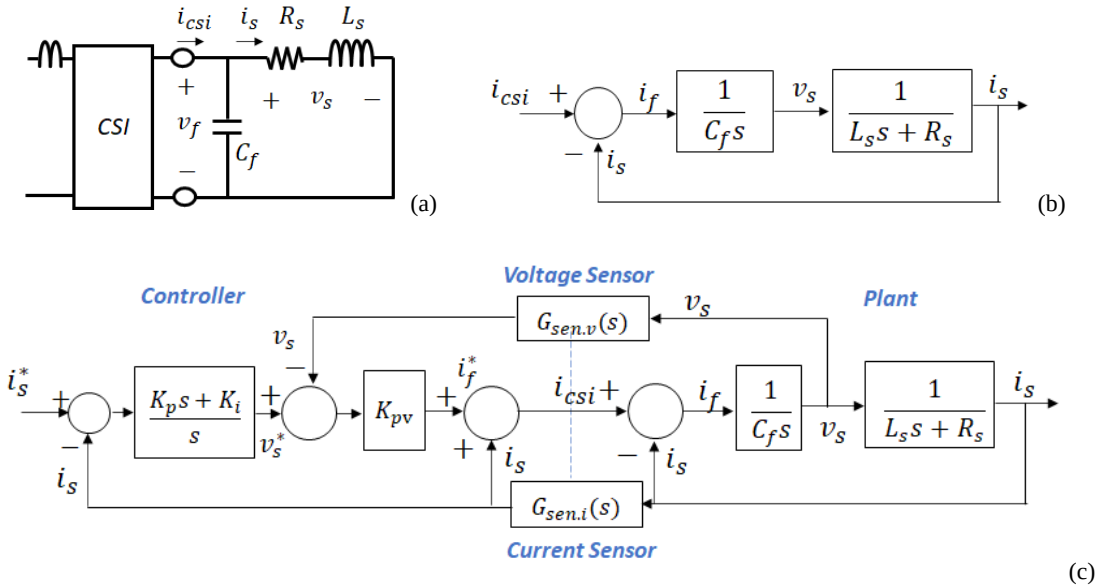

Fig. 2: (a) shows the equivalent model of the single-phase current source inverter with RL load. (b) the two-stage modeling of the plant and the transfer function (c) the conventional current controller in the continuous time domain.

Recent our studies [7, 8] have proposed a simplified controller that eliminates the need for ac current sensors. The proposed controller demonstrates similar characteristics to the controller previously studied [6]. This paper presents an approach for hardware implementation of this simplified controller and assesses its performance.

II. System Description of Current Source Inverter

The AC machine drive system, fed by a Current Source Inverter (CSI), can be modeled in the synchronous reference frame using equations (1)-(3). To capture the behavior of machines like Permanent Magnet Synchronous Machines (PMSM) or Synchronous Reluctance Machines, the voltage and current equations of the AC machine are employed for modeling from Fig. 3.

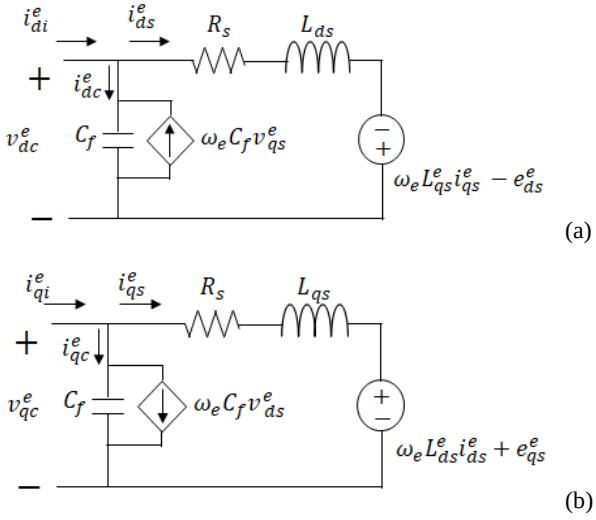

Fig. 3. The equivalent circuit of a Current Source Inverter (CSI) incorporating the AC motor system and capacitor filter can be represented in the e synchronous reference frame. (a) d-axis equivalent circuit. (b) q-axis equivalent circuit.

$$\begin{bmatrix} i^e_{di} \\ i^e_{qi} \end{bmatrix} = \begin{bmatrix} i^e_{ds} \\ i^e_{qs} \end{bmatrix} + \begin{bmatrix} i^e_{dc} \\ i^e_{qc} \end{bmatrix} \tag{1}$$

$$\begin{bmatrix} i^e_{dc} \\ i^e_{qc} \end{bmatrix} = \begin{bmatrix} \rho C_f & -\omega_e C_f \\ \omega_e C_f & \rho C_f \end{bmatrix} \begin{bmatrix} v^e_{dc} \\ v^e_{qc} \end{bmatrix} \tag{2}$$

$$\begin{bmatrix} v^e_{dc} \\ v^e_{qc} \end{bmatrix} = \begin{bmatrix} R_s + \rho L_{ds} & -\omega_e L_{qs} \\ \omega_e L_{ds} & R_s + \rho L_{qs} \end{bmatrix} \begin{bmatrix} i^e_{ds} \\ i^e_{qs} \end{bmatrix} + \begin{bmatrix} e^e_{ds} \\ e^e_{qs} \end{bmatrix} \tag{3}$$

where i^e_{dqi} are d- and q-axes output current of a CSI, i^e_{dqs} denotes d- and q-axes stator current of an ac machine, i^e_{dqc} denotes d- and q-axes stator current of an output filter capacitor, v^e_{dqc} represent d- and q-axes voltage of an output filter capacitor, C_f is an output filter capacitor of a CSI, R_s is a stator resistance of an ac machine, L_{dqs} are d- and q-axes synchronous inductance of an ac machine, ω_e represents a synchronous angular speed of an ac machine, e^e_{dqs} denote a back-emf voltage of an ac machine, and ρ is a differential operator i.e. d/dt. And superscripts "s" and "e" denote stationary and synchronous reference frame.

III. Design of Current Controller

By analyzing the block diagrams shown in Figure 2(a) and Figure 2(b), we can derive the transfer function of the single-phase Current Source Inverter (CSI) plant, denoted as

$$G_p(s) = \frac{I_s(s)}{I_{CSI}(s)} = \frac{\frac{1}{L_s C_f}}{s^2 + s\frac{R_s}{L_s} + \frac{1}{L_s C_f}} \tag{4}$$

Fig. 4. illustrates the bode plot of the transfer function $G_p(s)$ for the given parameters listed in Table I. Notley,

the plot examines three distinct values of the output filter capacitance C_f. Based on the bode diagram of Fig. 4, the intrinsic characteristic of the CSI has almost 0 dB gain at lower frequencies than approximately 0.3 $f_{resonant}$. Hence, when the resonance frequency is potentially reduced, it is possible for the output current of the Current Source Inverter (CSI) and the input current of the load to become equal (i.e., $I_{CSI} \approx I_s$) [6].

To prevent resonance frequency in a CSI with a AC load, one approach in physical is to use a small filter capacitance that raises the resonance frequency as high as possible to avoid interfering with the desired control band. Another method involves increasing load resistance to attenuate the resonance. However, these solutions have limitations due to the ripple current and their impact on system efficiency and heat generation, especially when employing SiC MOSFETs to increase the switching frequency.

Therefore, the main concept is to significantly raise the switching frequency by employing SiC MOSFETs. This allows the resonance frequency to be set above the required control band for AC load control. Additionally, since the output current of the CSI matches the load current (such as the stator current in motors), it becomes possible to implement a virtual damping resistance solely through a digital controller that can be designed to utilize voltage detection across the filter capacitor. This controller can eliminate the need for current sensors on the AC load.

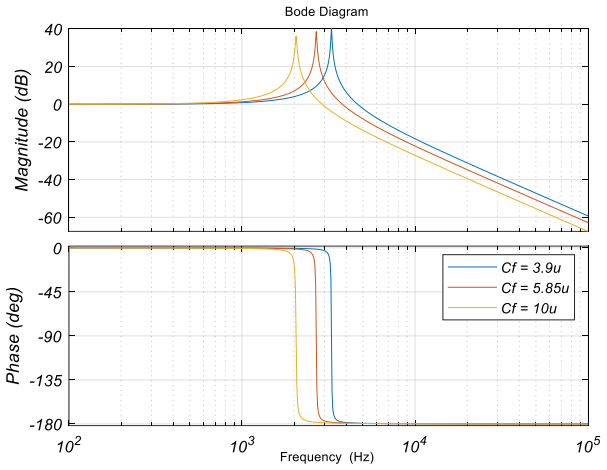

Fig. 4. Bode plot of the single-phase CSI with RL load $G_p(s)$ transfer function for different values of output filter capacitance.

TABLE I. PARAMETERS OF CSI WITH RL LOAD

	Parameter	Values	Unit
Load	Phase Inductance (L_s)	600	uH
	Phase Resistance (R_s)	0.12	Ω
Buck-CSI	Switching Frequnecy	80	kHz
	Filter capacitor	5.85	uF
	Input DC current source	1	A
	Overlap Time	313	ns

A. *Active Damping Controller for the CSI*

The block diagram depicted in Figure 5 represents an ideal implementation of the virtual resistance in a CSI drive, eliminating the need for an AC current sensor. In this figure, $\widehat{C_f}$ represents the estimated filter capacitance, $\widehat{L_s}$ is the estimated load inductance (motor phase inductance), and $\widehat{R_s}$ denotes the load resistance (motor phase resistance) [7, 8].

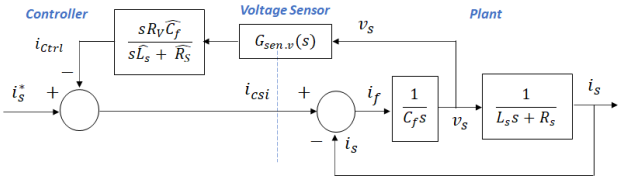

Fig. 5. The block diagram of proposed controller and plant which has only voltage sensors.

$$G_1(s) = \frac{1}{sC_f} \tag{5}$$

$$G_2(s) = \frac{1}{sL_s + R_s} \tag{6}$$

$$C(s) = \frac{I_{Ctrl}(s)}{V_S(s)} = \frac{sR_V\widehat{C_f}}{s\widehat{L_s} + \widehat{R_s}} = \frac{\frac{sR_V\widehat{C_f}}{\widehat{L_s}}}{s + \frac{\widehat{R_s}}{\widehat{L_s}}} \tag{7}$$

$$CL(s) = \frac{I_S(s)}{I_S^*(s)} = \frac{\frac{G_1(s)\,G_2(s)}{1 + G_1(s)\,C(s)}}{1 + \frac{G_1(s)G_2(s)}{1 + G_1(s)\,C(s)}} = \frac{\frac{1}{L_sC_f}}{s^2 + s\frac{(R_s + R_V)}{L_s} + \frac{1}{L_sC_f}} \tag{8}$$

A second-order system incorporating a virtual damping resistance can be derived using the formulas derived equations (5) to (8) in the continuous time domain. I_S^* represents a desired target current in (8). From (8), we can calculate the pole locations of the second-order system as

$$Pole = -\frac{R_v + R_s}{2L_s} \pm \frac{1}{2}\sqrt{\frac{(R_v + R_s)^2}{L_s^2} - \frac{4}{L_sC_f}} \tag{9}$$

$$\frac{(R_v + R_s)^2}{L_s^2} - \frac{4}{L_sC_f} = 0\,, \quad R_v + R_s = 2\sqrt{\frac{L_s}{C_f}} \tag{10}$$

In order to achieve a virtual resistor with the fastest response and no overshooting, corresponding to a critically damped system, a pole-zero configuration can be obtained. By equation (10) and the parameters provided in Table I, the value of R_v can be calculated to be approximately 20.2Ω. Fig. 6 shows the step response and the migration of the poles/zeros of the closed-loop transfer function $CL(s)$ when varying the virtual resistance.

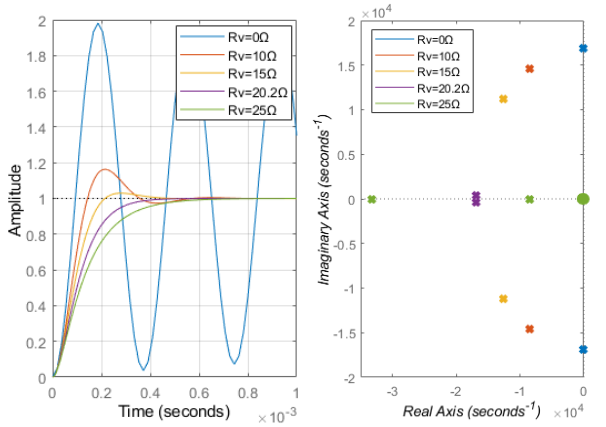

(a) (b)

Fig. 6. Impact of different virtual resistance R_v on the CSI-AC load drive: (a) unit step response, (b) pole-zero map.

B. Current Controller in synchronous reference frame

As mentioned in the previous section II, our ultimate objective is to apply the controller to a three-phase motor system. To achieve this, the previously designed controller can be extended by utilizing a synchronous reference frame. The desired system response in the synchronous reference frame can be summarized as described in equation (11).

$$\begin{bmatrix} i_{ds}^e \\ i_{qs}^e \end{bmatrix} = \begin{bmatrix} \frac{\frac{1}{C_f L_{ds}}}{s^2+s\frac{(R_s+R_{vd})}{L_{ds}}+\frac{1}{C_f L_{ds}}} & 0 \\ 0 & \frac{\frac{1}{C_f L_{qs}}}{s^2+\rho\frac{(R_s+R_{vq})}{L_{qs}}+\frac{1}{C_f L_{qs}}} \end{bmatrix} \begin{bmatrix} i_{ds}^{e*}+i_{dctrl}^e \\ i_{qs}^{e*}+i_{qctrl}^e \end{bmatrix} \quad (11)$$

R_{vd} and R_{vq} are the d- and q-axes virtual resistance, respectively. $i_{daqctrl}^e$ denotes the controller and i_{daqs}^{e*} denotes the desired target current.

To achieve the desired response like (11), the controller has to compensate the coupling term of the d-q synchronous reference frame.

$$\begin{bmatrix} i_{dc}^e \\ i_{qc}^e \end{bmatrix} = \begin{bmatrix} sC_f & 0 \\ 0 & sC_f \end{bmatrix} \begin{bmatrix} v_{dc}^e \\ v_{qc}^e \end{bmatrix} + \begin{bmatrix} 0 & -\omega_e C_f \\ \omega_e C_f & 0 \end{bmatrix} \begin{bmatrix} v_{dc}^e \\ v_{qc}^e \end{bmatrix}$$

$$= \begin{bmatrix} sC_f & 0 \\ 0 & sC_f \end{bmatrix} \begin{bmatrix} v_{dc}^e \\ v_{qc}^e \end{bmatrix} + \begin{bmatrix} v_{dc.ff}^e \\ v_{qc.ff}^e \end{bmatrix} \quad (12)$$

$$\begin{bmatrix} v_{dc.ff}^e \\ v_{qc.ff}^e \end{bmatrix} = \begin{bmatrix} 0 & -\omega_e \widehat{C_f} \\ \omega_e \widehat{C_f} & 0 \end{bmatrix} \begin{bmatrix} v_{dc}^e \\ v_{qc}^e \end{bmatrix} \quad (13)$$

From (2), it is possible to separate the coupling term, as shown in equation (12). Furthermore, the decoupling method can be accomplished by utilizing the feed-forward compensator provided in equation (13). Additionally, by employing Equations (3) and (12), the system can be rearranged and organized as depicted in (14). Furthermore, utilizing a feed-forward compensator, the relationship between the desired current and the resulting current, as illustrated in (11), can be controlled and organized as shown in (15).

$$\begin{bmatrix} i_{di}^e \\ i_{qi}^e \end{bmatrix} = \begin{bmatrix} i_{ds}^e \\ i_{qs}^e \end{bmatrix} + \begin{bmatrix} sC_f & 0 \\ 0 & sC_f \end{bmatrix} \begin{bmatrix} v_{dc}^e \\ v_{qc}^e \end{bmatrix} + \begin{bmatrix} v_{dc.ff}^e \\ v_{qc.ff}^e \end{bmatrix} \quad (14)$$

$$\begin{bmatrix} i_{ds}^{e*} \\ i_{qs}^{e*} \end{bmatrix} = \begin{bmatrix} i_{di}^e \\ i_{qi}^e \end{bmatrix} - \begin{bmatrix} i_{d.ctrl}^e \\ i_{q.ctrl}^e \end{bmatrix} - \begin{bmatrix} v_{dc.ff}^e \\ v_{qc.ff}^e \end{bmatrix} \quad (15)$$

$$\begin{bmatrix} i_{ds}^{e*} \\ i_{qs}^{e*} \end{bmatrix} = \begin{bmatrix} 1+sC_fR_s+s^2L_{ds}C_f & -sC_f\omega_e L_{qs} \\ sC_f\omega_e L_{ds} & 1+sC_fR_s+s^2C_fL_{qs} \end{bmatrix} \begin{bmatrix} i_{ds}^e \\ i_{qs}^e \end{bmatrix} + \begin{bmatrix} sC_f & 0 \\ 0 & sC_f \end{bmatrix} \begin{bmatrix} e_{ds}^e \\ e_{qs}^e \end{bmatrix} - \begin{bmatrix} i_{d.ctrl}^e \\ i_{q.ctrl}^e \end{bmatrix} \quad (16)$$

When the d-q coupling of the filter capacitor is effectively compensated using the feed-forward compensator, the system can be arranged as illustrated in (16). In most cases, the induced voltage of the motor, represented by e_{dqs}^e, does not exhibit significant changes due to mechanical inertia during high-speed sampling. As a result, it can be disregarded. Consequently, in the synchronous coordinate system, the current controller can be organized according to the representation shown in (17).

$$\begin{bmatrix} i_{d.ctrl}^e \\ i_{q.ctrl}^e \end{bmatrix} = \begin{bmatrix} \frac{-s\widehat{C_f}R_{vd}}{\widehat{R_s}+s\widehat{L_{ds}}} & 0 \\ 0 & \frac{-s\widehat{C_f}R_{vq}}{\widehat{R_s}+s\widehat{L_{qs}}} \end{bmatrix} \begin{bmatrix} v_{dc}^e - e_{ds}^e \\ v_{qc}^e - e_{qs}^e \end{bmatrix} + \begin{bmatrix} 0 & -\frac{s\widehat{C_f}\omega_e\widehat{L_{qs}}}{\widehat{R_s}+\omega_e\widehat{L_{qs}}} \\ \frac{s\widehat{C_f}\omega_e\widehat{L_{ds}}}{\widehat{R_s}+\omega_e\widehat{L_{ds}}} & 0 \end{bmatrix} \begin{bmatrix} v_{dc}^e - e_{ds}^e \\ v_{qc}^e - e_{qs}^e \end{bmatrix} \quad (17)$$

C. Digital Controller Design

Fig. 7 shows the discrete-time domain model of the complete CSI-AC motor drive with the virtual resistance feedback without ac current sensor. The transfer function C(z) represents the control algorithm incorporating the virtual resistance, as depicted in equation (18). It is worth noting that the block diagram includes a time delay z^{-1} to accommodate the delay between the sampling time and the update of the PWM duty cycle.

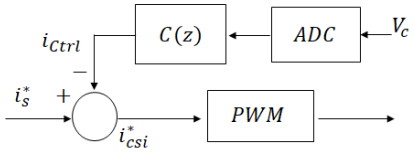

Fig. 7. Discrete time domain block diagram of the CSI-AC load drive with virtual resistance feedback in stationary reference frame.

$$C(z) = (1 - z^{-1})Z\{\frac{C(s)}{s}\} = \frac{\frac{R_V \widehat{C_f}}{\widehat{L_s}}(z-1)}{z - e^{-\frac{\widehat{R_S}}{\widehat{L_s}}T_s}} \quad (18)$$

$$CL(z) = \frac{z^{-1}\, G_1(z)\, G_2(z)}{1 + z^{-1}\, G_1(z)\, C(z) + z^{-1} G_1(z) G_2(z)} \quad (19)$$

In (19), $CL(z)$ shows the close loop system in the discrete time domain with time delay. In Fig. 8, the response characteristics in relation to the digital delay are depicted. However, instability occurs when the digital delay exceeds a 2-sample delay.

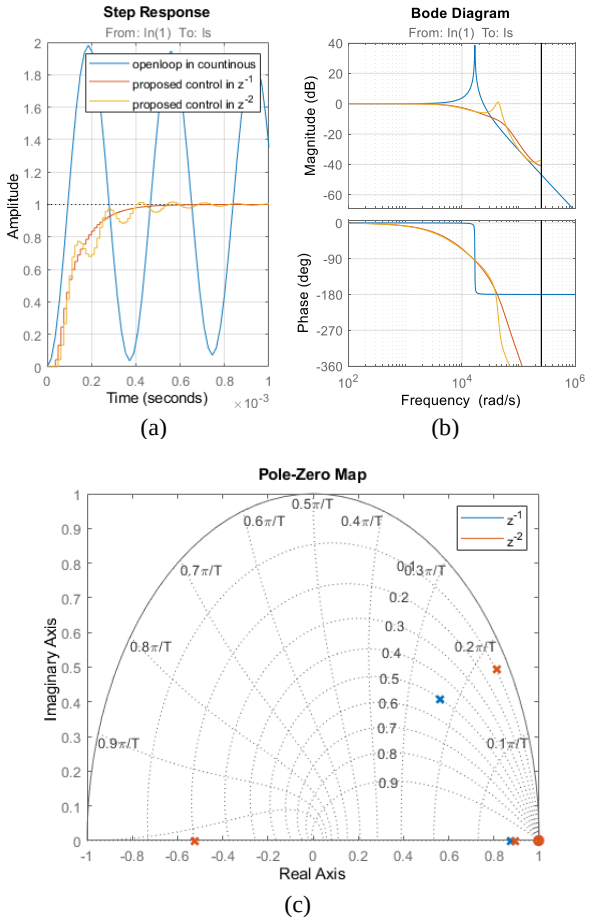

(a) (b) (c)

Fig. 8. Impact of different sample delay on the CSI-AC load drive CL(z) transfer function: (a) step response, (b) bode diagram, (c) pole-zero plot

The decoupling term in equation (17) includes a differential component that may introduce unstable from noise or other disturbances in the digital system. To address this issue, a digital filter was employed to mitigate the differential term, as illustrated in equation (20).

$$C_{PF}(z) = \frac{s}{s + \omega_c}\Big|_{s=\frac{2z-1}{Tz+1}} = \frac{z-1}{\left(1 + \frac{\omega_c T_s}{2}\right)z - \left(1 - \frac{\omega_c T_s}{2}\right)} \quad (20)$$

Consequently, the proposed digital controller can be structured as depicted in equation (21). However, digital systems can experience additional digital delays due to various factors such as noise. To compensate for this, an all-pass filter was implemented as a means of addressing the issue. All-pass filters maintain a consistent gain while allowing for phase adjustments.

$$\boldsymbol{C(z)} = \begin{bmatrix} \frac{\frac{R_{Vd}\widehat{C_f}}{\widehat{L_{ds}}}(z-1)}{z - e^{-\frac{\widehat{R_S}}{\widehat{L_{ds}}}T_s}} & \frac{\widehat{C_f}\omega_e \widehat{L_{qs}}}{\widehat{R_s} + \omega_e \widehat{L_{qs}}} C_{PF}(z) \\ \frac{-\widehat{C_f}\omega_e \widehat{L_{ds}}}{\widehat{R_s} + \omega_e \widehat{L_{ds}}} C_{PF}(z) & \frac{\frac{R_{Vq}\widehat{C_f}}{\widehat{L_{qs}}}(z-1)}{z - e^{-\frac{\widehat{R_S}}{\widehat{L_{qs}}}T_s}} \end{bmatrix} \begin{bmatrix} v_{dc}^e - e_{ds}^e \\ v_{qc}^e - e_{qs}^e \end{bmatrix} \quad (21)$$

$$APF(z) = \frac{z^{-1} - \gamma}{1 - \gamma\, z^{-1}} \quad (22)$$

The comprehensive current controller, incorporating the all-pass filter as shown in equation (22), can be observed in Fig. 9(a). The complete system configuration is depicted in Fig. 9(b).

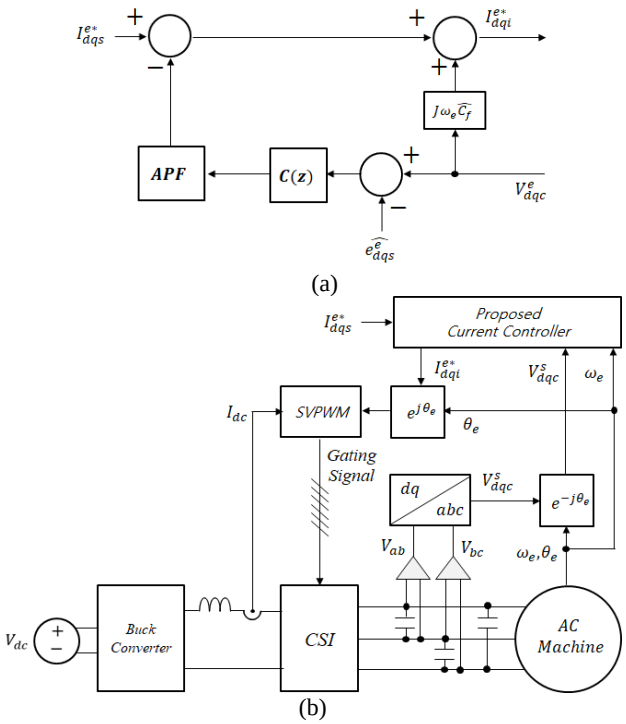

(a) (b)

Fig. 9. The block diagram of proposed controller and system which has only voltage sensors in the e synchronous reference frame (a) the proposed current controller with all pass filter (b) the overall control system.

The proposed controller is output through the PWM implemented as shown in Fig. 10 using FPGA. The CSI using SiC MOSFET has a very short turn-off time compared to the IGBT-based CSI, so attention shall be paid to the over-lap time design to avoid open-circuit

failure. The design and control characteristics of these power switches have been extensively analyzed in previous studies [9, 10].

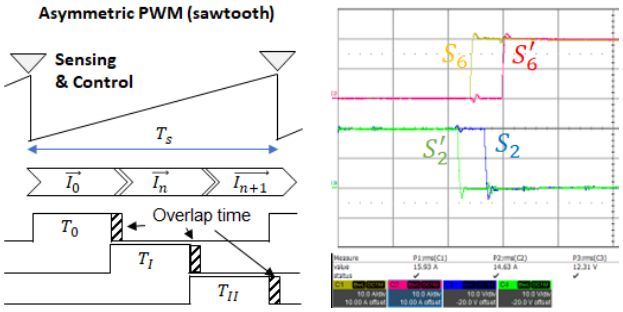

(a) (b)

Fig. 10. Implementation of PWM for CSI with Overlap Time and Dead Time using FPGA: (a) concept of PWM, (b) measured PWM signal.

IV. Experimental Results

In the previous research [9, 10], a prototype was developed and depicted in Fig. 11, featuring a bi-directional SiC MOSFET switch designed for CSI applications. Initially, the current controller was tested under an inductor load to conduct the preliminary tests. The parameters used for these tests align with the values provided in Table I.

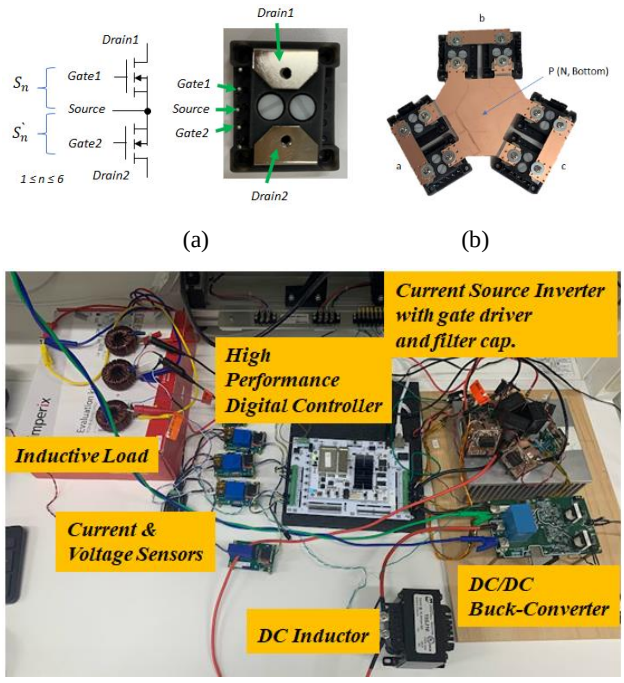

(a) (b)

(c)

Fig. 11. The experimental configuration. (a) IMS-based bi-directional SiC MOSFET switch, (b) PCB prototype for the three-phase CSI, and (c) the overall experimental setup.

Fig. 12(a) exhibits the response characteristics of an open-loop system with a DC current of 1A, where no controller is employed. It can be observed that the system displays a resonance frequency of approximately 2.8 kHz, consistent with the system parameters. Subsequently, the proposed controller depicted in Fig. 12(b) was applied, resulting in the attenuation of the resonance frequency when the same DC current was applied. However, due to sensing delays and the characteristics of the all-pass filter, complete control over overshooting could not be achieved. Nevertheless, a stable response within approximately 600us was confirmed. Additionally, Fig. 12(c) and (d) validate that the controller effectively attenuates and controls the resonance frequency even at a fundamental frequency of 100 Hz. Finally, Fig. 12(e) and (f) demonstrate that the controller exhibits an appropriate response even at a fundamental frequency of 1 kHz.

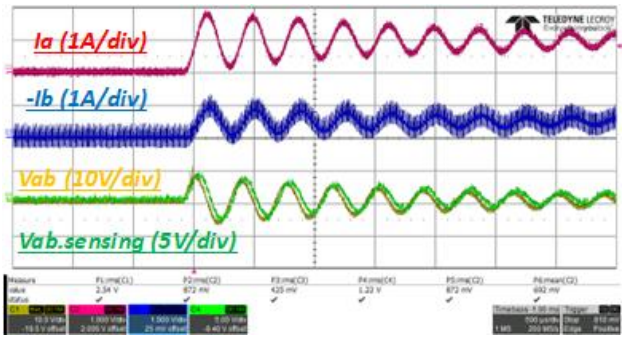

(a)

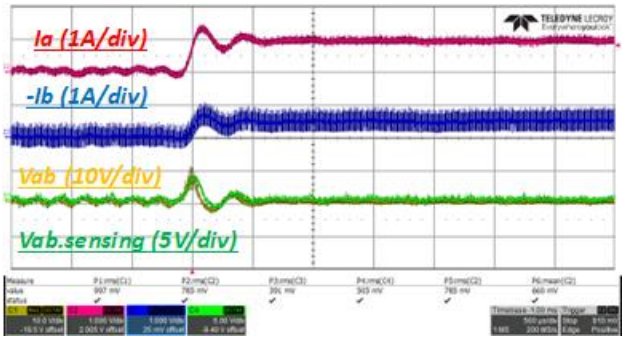

(b)

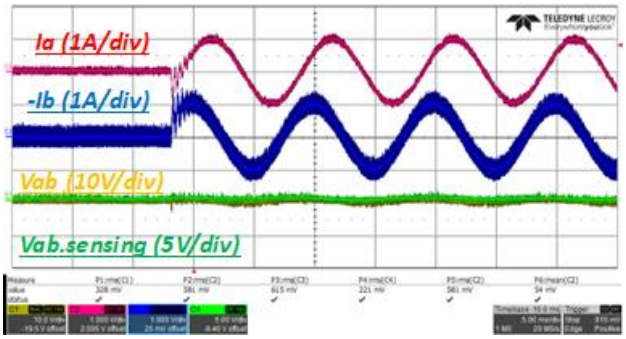

(c)

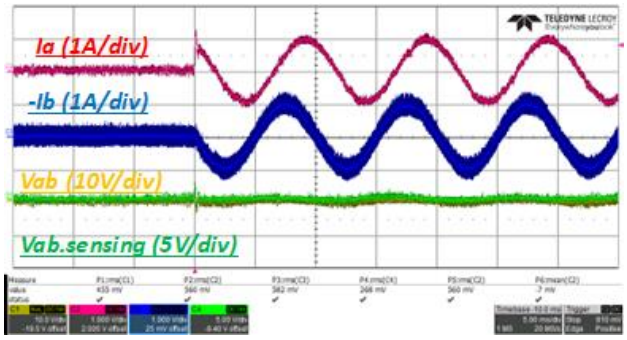

(d)

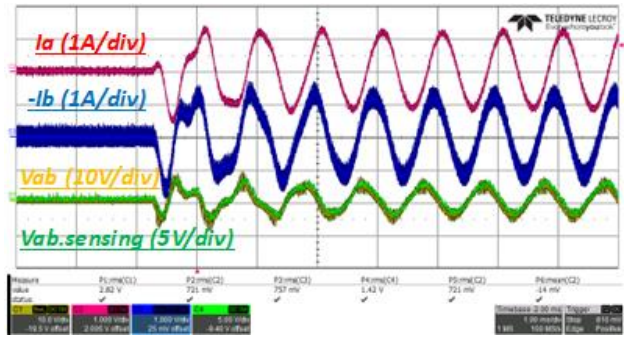

(e)

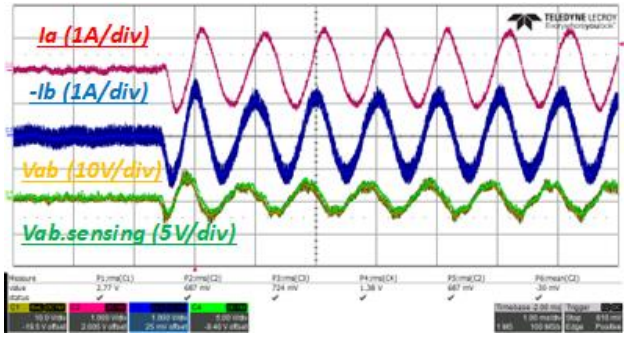

(f)

Fig. 12. The experimental result (a) DC 1A open-loop response, (b) DC 1A with the proposed controller, (c) fout = 100Hz Ids = 1A without the controller, (d) fout = 100Hz, Ids = 1A, with the proposed controller, (e) fout = 1kHz, Ids = 1A without the controller, and (f) fout = 1kHz, Ids = 1A with the proposed controller.

V. Conclusions

This paper presents the design of digital control system, conceived specifically for the realization of advanced CSI topologies. A digital controller was introduced based on a three-phase synchronous reference frame, and a controller incorporating an all-pass filter was proposed and experimentally validated to compensate for digital delays. While a voltage sensor-based controller was specifically designed, it was unable to completely eliminate overshoot response. However, the results confirmed the potential for high-speed control utilizing SiC MOSFETs. Moving forward, future endeavors will focus on exploring further enhancements through motor applications and conducting additional experiments.

References

[1] Abebe, R., Vakil, G., Lo Calzo, G., Cox, T., Lambert, S., Johnson, M., Gerada, C., Mecrow, B.: 'Integrated motor drives: state of the art and future trends', IET Electric Power Applications, 10, (8), pp. 757–774,.2015.

[2] R. A. Torres, H. Dai, W. Lee, T. M. Jahns and B. Sarlioglu, "Current-Source Inverters for Integrated Motor Drives using Wide-Bandgap Power Switches," 2018 IEEE Transportation Electrification Conference and Expo (ITEC), 2018, pp. 1002-1008.

[3] H. Dai, R. A. Torres, T. M. Jahns and B. Sarlioglu, "An H8 Current-Source Inverter using Wide Bandgap Bidirectional Switches," 2019 IEEE Energy Conversion Congress and Exposition (ECCE), 2019, pp. 2361-2368.

[4] H. -J. Lee, S. Jung and S. -K. Sul, "A current controller design for current source inverter-fed PMSM drive system," 8th International Conference on Power Electronics - ECCE Asia, Jeju, Korea (South), 2011, pp. 1364-1370, doi: 10.1109/ICPE.2011.5944414.

[5] H. -J. Lee, S. Jung and S. -K. Sul, "A Current Controller Design for Current Source Inverter-Fed AC Machine Drive System," in IEEE Transactions on Power Electronics, vol. 28, no. 3, pp. 1366-1381, March 2013, doi: 10.1109/TPEL.2012.2208985.

[6] R. A. Torres, H. Dai, W. Lee, T. M. Jahns and B. Sarlioglu, "A Simple and Robust Controller Design for High-Frequency WBG-Based Current-Source-Inverter-Fed.AC Motor Drive," 2020 IEEE Transportation Electrification Conference & Expo (ITEC), 2020, pp. 111-117.

[7] Lee Y, Castellazzi A. Implementation options of a fully SiC Buck-CSI for advanced motor drive application. In2022 24th European Conference on Power Electronics and Applications (EPE'22 ECCE Europe) 2022 Sep 5 (pp. P-1). IEEE.

[8] Lee Y, Castellazzi A. Discrete-time optimization of current-sensor-less control for a high-frequency all-SiC CSI converter. In2022 25th International Conference on Electrical Machines and Systems (ICEMS) 2022 Dec 2 (to be presented). IEEE.

[9] Y. Lee, A. Castellazzi, S. Avilès, C. Duchesne and P. Lasserre, "SiC MOSFET bi-directional switch IMS module design," 2023 35th International Symposium on Power Semiconductor Devices and ICs (ISPSD), Hong Kong, 2023, pp. 52-55, doi: 10.1109/ISPSD57135.2023.10147615.

[10] Y Lee and A. Castellazzi, "IMS-based integrated SiC-MOSFET bi-directional switches for advanced CSI implementation", Proc. ECCE-Asia 2023, May 22-25, 2023.